IGRINS NEAR-IR HIGH-RESOLUTION SPECTROSCOPY OF MULTIPLE JETS AROUND LkHα 234[*]

HEEYOUNG OH[1,2], TAE-SOO PYO[3,4], IN-SOO YUK[1], BYEONG-GON PARK[1,2], CHAN PARK[1], MOO-YOUNG CHUN[1], SOOJONG PAK[5],
KANG-MIN KIM[1], JAE SOK OH[1], UEEJEONG JEONG[1,6], YOUNG SAM YU[1], JAE-JOON LEE[1], HWIHYUN KIM[1,7], NARAE HWANG[1],
KYLE KAPLAN[7], MICHAEL PAVEL[7], GREGORY MACE[7], HYE-IN LEE[5], HUYNH ANH NGUYEN LE[5], SUNGHO LEE[1],
AND DANIEL T. JAFFE[7]

[1] Korea Astronomy and Space Science Institute, 776 Daedeok-daero, Yuseong-gu, Daejeon 305-348, Korea; hyoh@kasi.re.kr
[2] Korea University of Science and Technology, 217 Gajeong-ro, Yuseong-gu, Daejeon 305-350, Korea
[3] Subaru Telescope, National Astronomical Observatory of Japan, 650 North A'ohoku Place, Hilo, HI 96720, USA
[4] School of Mathematical and Physical Science, SOKENDAI (The Graduate University for Advanced Studies), Hayama, Kanagawa 240-0193, Japan
[5] School of Space Research and Institute of Natural Sciences, Kyung Hee University, 1732 Deogyeong-daero, Giheung-gu, Yongin-si, Gyeonggi-do 17104, Korea
[6] Center for Atmospheric Remote Sensing (CARE), Kyungpook National University, 80 Daehakro, Bukgu, Daegu, 702-701, Korea
[7] Department of Astronomy, University of Texas at Austin, Austin, TX, USA

ABSTRACT

We present the results of high-resolution near-IR spectroscopy toward the multiple outflows around the Herbig Be star LkHα 234 using the Immersion Grating Infrared Spectrograph. Previous studies indicate that the region around LkHα 234 is complex, with several embedded young stellar objects and the outflows associated with them. In simultaneous H- and K-band spectra from HH 167, we detected 5 [Fe II] and 14 H$_2$ emission lines. We revealed a new [Fe II] jet driven by radio continuum source VLA 3B. Position–velocity diagrams of the H$_2$ 1−0 S(1) $\lambda 2.122\,\mu$m line show multiple velocity peaks. The kinematics may be explained by a geometrical bow shock model. We detected a component of H$_2$ emission at the systemic velocity ($V_{\mathrm{LSR}} = -10.2\,\mathrm{km\,s^{-1}}$) along the whole slit in all slit positions, which may arise from the ambient photodissociation region. Low-velocity gas dominates the molecular hydrogen emission from knots A and B in HH 167, which is close to the systemic velocity; [Fe II] emission lines are detected farther from the systemic velocity, at $V_{\mathrm{LSR}} = -100$–$-130\,\mathrm{km\,s^{-1}}$. We infer that the H$_2$ emission arises from shocked gas entrained by a high-velocity outflow. Population diagrams of H$_2$ lines imply that the gas is thermalized at a temperature of 2500–3000 K and the emission results from shock excitation.

Key words: ISM: individual objects (HH 167) – ISM: jets and outflows – stars: formation – stars: individual (LkHα 234) – stars: variables: T Tauri, Herbig Ae/Be – techniques: spectroscopic

1. INTRODUCTION

LkHα 234 (V373 Cep) is a B7-type Herbig Be star in the cluster NGC 7129 ($D = 1.25$ kpc, Shevchenko & Yakubov 1989). The star is ∼8.5 $M_\odot$, ∼1700 $L_\odot$ (Hillenbrand et al. 1992), and has an age of ∼10^5 years (Strom et al. 1972; Fuente et al. 2001). LkHα 234 is bright in far-IR bands and is surrounded by reflection nebulae (Bechis et al. 1978; Bertout 1987). It is one of the objects in the catalog of embedded clusters (Lada & Lada 2003), and is a well-known water maser emission source (Cesarsky et al. 1978; Rodriguez et al. 1987; Trinidad et al. 2004; Marvel 2005; Bae et al. 2011).

The LkHα 234 region is complex, with multiple outflows from different young stellar objects (YSOs). Edwards & Snell (1983) discovered a large-scale outflow in $J = 1$−0 ^{12}CO, which is mostly redshifted with low velocity (∼10 km s^{-1}), to the northeast of LkHα 234. Shocked H$_2$ flows are also detected in the CO outflow region (Eislöffel 2000). Mid-IR spectroscopy showed that this shocked H$_2$ is collisionally excited by a J-type shock (Morris et al. 2004).

Ray et al. (1990) found a blueshifted optical [S II] jet (HH 167), which extends more than 30″ with a position angle (P.A.) of 252°. Ray et al. (1990) argue that this jet is the counterpart of the red CO lobe. Schultz et al. (1995) showed that there is near-IR H$_2$ emission at the position of the [S II] jet, and Cabrit et al. (1997) confirmed an H$_2$ jet in images with high angular resolution. The H$_2$ jet coincides with knots A, B, and C of the

[S II] jet (Ray et al. 1990). Kato et al. (2011) noticed two jet-like features in their stellar coronagraphic images in the J- and H-bands. One of the jet-like features is coincident with a "green blob" in the middle of the reflection nebula shown in their JHK color composite image. The position of the green blob is in agreement with the [Fe II] emission in Schultz et al. (1995). In addition, McGroarty et al. (2004) suggested a parsec-scale jet over ∼22′ (∼8 pc) as projected on the sky, including HH 815–822 and HH 103A. In Figure 1, we show the source candidates and the axes of outflows on the images taken from Kato et al. (2011) and Cabrit et al. (1997). Also, Table 3 in Kato et al. (2011) established the association of sources and source labels from previous studies, which helps the understanding of this region.

Polarimetric observations at 2 μm by Weintraub et al. (1994) revealed the existence of an embedded young stellar companion 3″ northwest of LkHα 234. Their polarization map also showed that the companion is the most likely illuminating source of the reflection nebula. Cabrit et al. (1997) detected a 10 μm source (IRS 6) at the position coinciding with the center of the polarization vectors in Weintraub et al. (1994). Polomski et al. (2002) also detected a mid-IR source NW at the position of IRS 6. Since the axis of the H$_2$ jet (P.A. = 227°) is not aimed at IRS 6, the possible existence of another embedded source was suggested. IRS 6 is not driving the H$_2$ jet, but it was regarded as the source of the CO/[S II] outflow (Cabrit et al. 1997; Fuente et al. 2001). Millimeter observations by Fuente et al. (2001) revealed a new embedded source, FIRS1-MM1 ∼4″ northeast of LkHα 234. FIRS1-MM1 lies within 1″
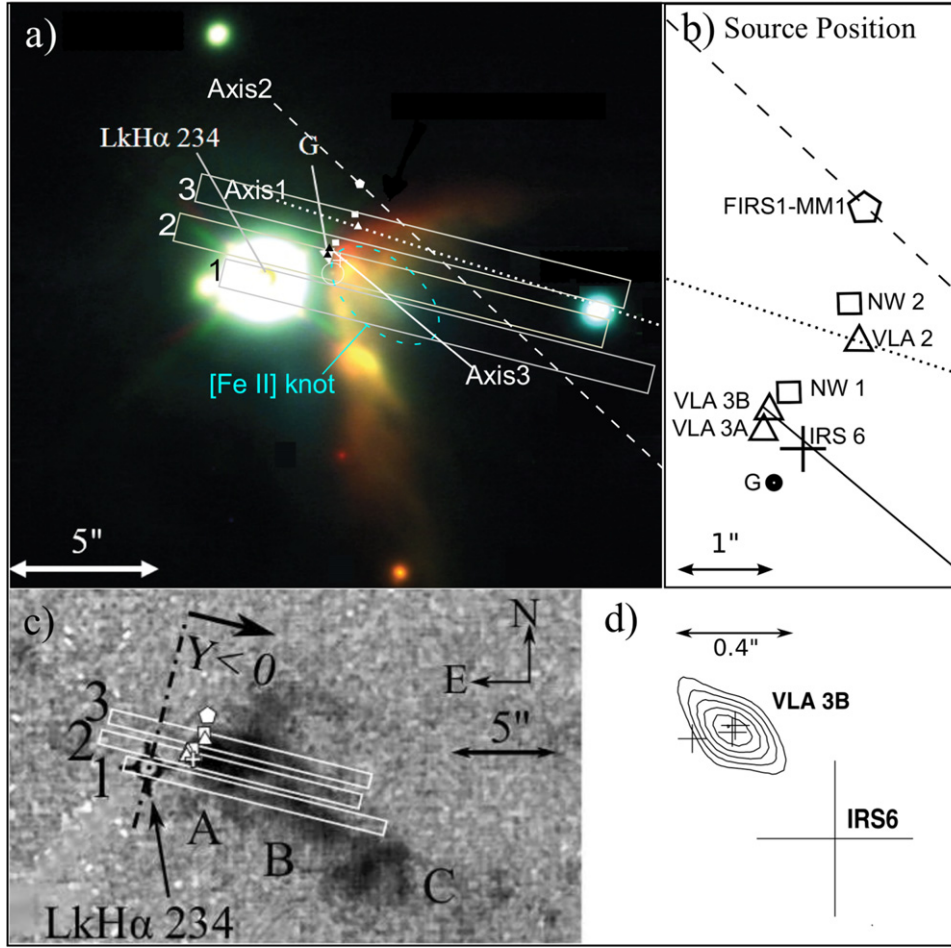
Figure 1. Key for the LkHα 234 region. (a) Three slit positions, outflow source candidates, and axes of outflows. (b) Zoom-in of source positions. The $1''0$ (W) $\times$ $14''8$ (L) slits at position angles of $256°$ are superposed on the *JHK* color composite image (Kato et al. 2011). The slit positions are numbered 1, 2, and 3 (SP 1, 2, and 3) from the bottom to the top in the figure. (c) The slit positions on the continuum-subtracted H_2 emission line image (Cabrit et al. 1997). The dash–dotted line represents the position of $Y = 0''$, and knots A, B, and C are shown. (d) Source-subtracted 3.6 cm map taken from Trinidad et al. (2004). FIRS1-MM1, VLA sources, mid-IR sources NW 1, NW 2, and IRS 6 are marked and a dashed ellipse shows the position of the bright [Fe II] knot detected at SP 1 and 2. The positional uncertainties of the sources are described in Section 1. The dotted, dashed, and solid lines marked as Axis1, Axis2, and Axis3 indicate axes of an optical [S II] jet, a near-IR H_2 jet, and an [Fe II] jet that is newly suggested in this study, respectively. Axis1 and Axis2 correspond to A1 and A2 of Fuente et al. (2001). Letter G is marked in the original image of Kato et al. (2011), indicating the YSO candidate.

of the jet axis, so it is suggested as the source of the H_2 jet (Fuente et al. 2001).

Many radio observations have shown strong continuum emission near LkHα 234 (e.g., Wilking et al. 1986; Skinner et al. 1993; Tofani et al. 1995). The strongest radio source, VLA 3, is associated with IRS 6. Trinidad et al. (2004) showed that VLA 3 is a binary system (3A and 3B) having thermal radio jets. In the 1.3 and 3.6 cm continua and H_2O maser observations, the water maser sources around another radio source, VLA 2, trace the axis of [S II] outflow. The proper motion of H_2O masers showed bipolar motions centered on VLA 2 along the axis of [S II] outflow. These suggested that VLA 2 is the driving source of [S II] outflow (Trinidad et al. 2004; Torrelles et al. 2014). Kato et al. (2011) detected NW 1 and 2 at the positions of IRS 6 and VLA 2, respectively, in a mid-IR observation.

In Figure 1, the positional uncertainties are less than $0''2$ and $0''05$ for the radio sources and the mid-IR sources (NW 1 and 2). For IRS 6, the cross indicates an uncertainty. We note that an additional error could be caused by astrometric matching between different observations, which is less than $0''5$.

From the previous studies (Cabrit et al. 1997; Fuente et al. 2001), we can say that the [S II] outflow is driven by VLA 2 (= NW 2) and that FIRS1-MM1 is well aligned with the near-IR H_2 jet axis. Currently there is no evidence of LkHα 234 itself being an outflow driving source.

A large fraction of stars form in binary or multiple-star systems (Duquennoy & Mayor 1991; Connelley et al. 2008a, 2008b; Reipurth et al. 2014, p. 267; Pineda et al. 2015). For all stars, outflows and mass-accretion are an essential part of their formation and early evolution (Hartigan et al. 1995). While studies of single star–disk systems have yielded much knowledge about outflows and mass-accretion from YSOs, the complicated nature of multiple-star systems makes it more difficult to understand their characteristics in detail. High-resolution spatial-kinematic analysis toward outflows in young multiple systems can help us to understand their complicated velocity distribution and physical conditions. In this paper, we report the first high-resolution near-IR spectroscopic observations of the multiple outflows around LkHα 234 using the recently developed Immersion GRating INfrared Spectrograph (IGRINS, Yuk et al. 2010; Park et al. 2014). We

detected emission lines from [Fe II] and in ro-vibrational transitions of H_2 including [Fe II] $\lambda 1.644\,\mu$m and H_2 1−0 S (1) $\lambda 2.122\,\mu$m lines. From our result, we suggest a newly confirmed [Fe II] outflow, possibly driven by VLA 3B. In Section 2, we describe the observations and data reduction. Section 3 shows the obtained position–velocity diagrams (PVDs) and line ratios. We discuss the characteristics of the [Fe II] and H_2 emission, and the driving sources of multiple outflows in Section 4. We summarize the results in Section 5.

2. OBSERVATION AND DATA REDUCTION

The data were obtained during a commissioning run of IGRINS mounted on the 2.7 m Harlan J. Smith Telescope at the McDonald Observatory of the University of Texas. The date of observation was 2014 July 13 (UT). IGRINS covers the whole H-band (1.49–1.80 μm) and K-band (1.96–2.46 μm) simultaneously, with a high spectral resolution R ($\lambda/\Delta\lambda$) of ~40,000 ($\Delta v = 7.5\,$km s^{-1} with ~3.5 pixels). Each H- and K-band camera uses a (2k × 2k) HAWAII-2RG array as a detector (Jeong et al. 2014; Oh et al. 2014). The pixel scale along the slit, which becomes larger in higher orders, was $0.''24$–$0.''29\,$pixel^{-1}. The slit size was $1.''0$ (W) × $14.''8$ (L). Auto-guiding was performed during each exposure with a K-band slit-viewing camera equipped with a (2k × 2k) HAWAII-2RG array (pixel scale $= 0.''12\,$pixel^{-1}). The guiding uncertainty on average was smaller than $0.''4$. The seeing condition was about $1.''1$ at in the K-band.

The observations were made at three slit positions covering LkHα 234 and HH 167. In Figure 1, the slit positions are marked on the JHK color composite and H_2 narrow-band images. The white rectangles represent slit positions 1, 2, and 3 (hereafter SP 1, 2, and 3). The P.A. of the slit was 256° in all positions. We confirmed the slit positions and P.A. by matching the positions of stars on the slit-view images and the 2MASS Ks image. The total on-source integration time was 600 s for each slit position. The sky frames were obtained with the same exposure time as on-source frames. We observed HR 6386 ($K = 6.52$, SpT = A0V) as a standard star. Th–Ar and halogen lamp frames were acquired for wavelength calibration and flat-fielding, respectively.

We performed the basic data reduction with the IGRINS Pipeline Package[8] (PLP). The PLP performs sky subtraction, flat-fielding, bad pixel correction, aperture extraction, and wavelength calibration. To make PVDs, we conducted additional processes on the data using IRAF (the Image Reduction and Analysis Facility). We resampled the spectra with a uniform wavelength interval per pixel along the dispersion direction using the TRANSFORM task (linearization). After we removed the Brackett series of absorption lines from the standard star spectra using the SPLOT task, we performed the wavelength sensitivity correction and flux calibration with standard star spectra. The telluric line correction was performed with the TELLURIC task. We used the BACKGROUND task to subtract the continuum emission from LkHα 234.

3. RESULT

In Figure 1(c), the $Y = 0''$ position along the slit is indicated with a dash–dotted line, which crosses the position of LkHα

---

234 in SP 1 and is perpendicular to the P.A. of the slits. The notation of knots A, B, and C is from Ray et al. (1990). Although the inclination angle of the jet is not known, the positional change of the knots on the sky plane is supposed to be small ($<1''$) due to the large distance from us (1.25 kpc). Figure 2 shows line profiles of all five detected [Fe II] emission lines and eight selected H_2 emission lines toward knot A at SP 1, 2, and 3. In Figure 3, we show the PVDs of the H_2 1−0 S(1) $\lambda 2.122\,\mu$m and [Fe II] $\lambda 1.644\,\mu$m lines at the three slit positions. The line profiles at $0.''5$ intervals along the Y direction are shown in Figure 4.

3.1. Line Profiles of [Fe II] and H_2 Emission

In Figure 2, the fluxes are integrated over knot A ($-6.''5 < Y < -0.''5$). The [Fe II] lines at SP 1 and 2 show similar profiles with a peak velocity ($v_{\rm peak}$) of ~ $-110\,$km s^{-1} and a shoulder toward lower velocity. At SP 3, only the [Fe II] $\lambda 1.644\,\mu$m line is detected. All H_2 lines show similar profiles at each slit position. At SP 1 and 3, the H_2 emission lines have asymmetric line profiles. At SP 1, the profiles peak at $V_{\rm LSR} \sim -11\,$km s^{-1} and show blueshifted wings. The profiles at SP 3 are asymmetric relative to the peak velocity ($V_{\rm LSR} \sim -13\,$km s^{-1}), showing a gradual slope on the red side of the line. At SP 2, they show double peaks at $V_{\rm LSR} = -30$ and $-5\,$km s^{-1}.

The [Fe II] and H_2 emission profiles differ significantly: H_2 emission lines are strong at low velocity, close to the systemic velocity of $V_{\rm LSR} = -10.2\,$km s^{-1} (Liu et al. 2011), while [Fe II] emission lines are prominent at higher velocity. In the following section, we compare [Fe II] $\lambda 1.644\,\mu$m and H_2 1−0 S (1) $\lambda 2.122\,\mu$m emission lines at each slit position in detail.

### 3.2. PVDs of H_2 1−0 S(1) $\lambda 2.122\,\mu$m and [Fe II] $\lambda 1.644\,\mu$m Emission

3.2.1. Slit Position 1 (SP 1)

In Figure 3, contours and color gradients represent H_2 and [Fe II] emission, respectively. SP 1 includes the southern part of knot A and the center of knot B, as shown in Figure 1. The H_2 emission in knot A shows multiple intensity peaks. We marked two strong peaks as A1 and A2. They are at $Y = -3.''5$ and $-4.''8$, and their peak velocities are ~ -25 and $-11\,$km s^{-1}, respectively. A weak, but high-velocity ($-110\,$km s^{-1}) emission is also detected at $Y = -5.''0$, at a similar position to knot A2. Velocity widths at half intensity ($v_{\rm FWHM}$) are ~37 and 23 km s^{-1} for A1 and A2, respectively. The $v_{\rm peak}$ of A2 is very similar to the systemic velocity (i.e., $-10.2\,$km s^{-1}). A plateau extending from knot A is shown at $Y = -5.''3$ and $V_{\rm LSR} = -50\,$km s^{-1}.

We detected a bright, high-velocity [Fe II] knot at $Y = -4.''7$ with a $v_{\rm peak} \sim -113\,$km s^{-1}. Its position and velocity are almost consistent with high-velocity H_2 emission at $Y = -5.''0$ mentioned above. The [Fe II] emission also shows an extended velocity component that peaks at $-73\,$km s^{-1}. The full width at zero intensity (FWZI) of the [Fe II] profile that contains both high-velocity and extended components is ~130 km s^{-1}. From their double-peak line profile (Figure 4), we estimated the velocity widths and peak intensities by a multiple-Gaussian fitting. $v_{\rm FWHM}$ are 33 and 41 km s^{-1} for high-velocity and extended components, respectively. The peak intensity level of the extended component is about three times weaker than that of the bright peak (~40σ).
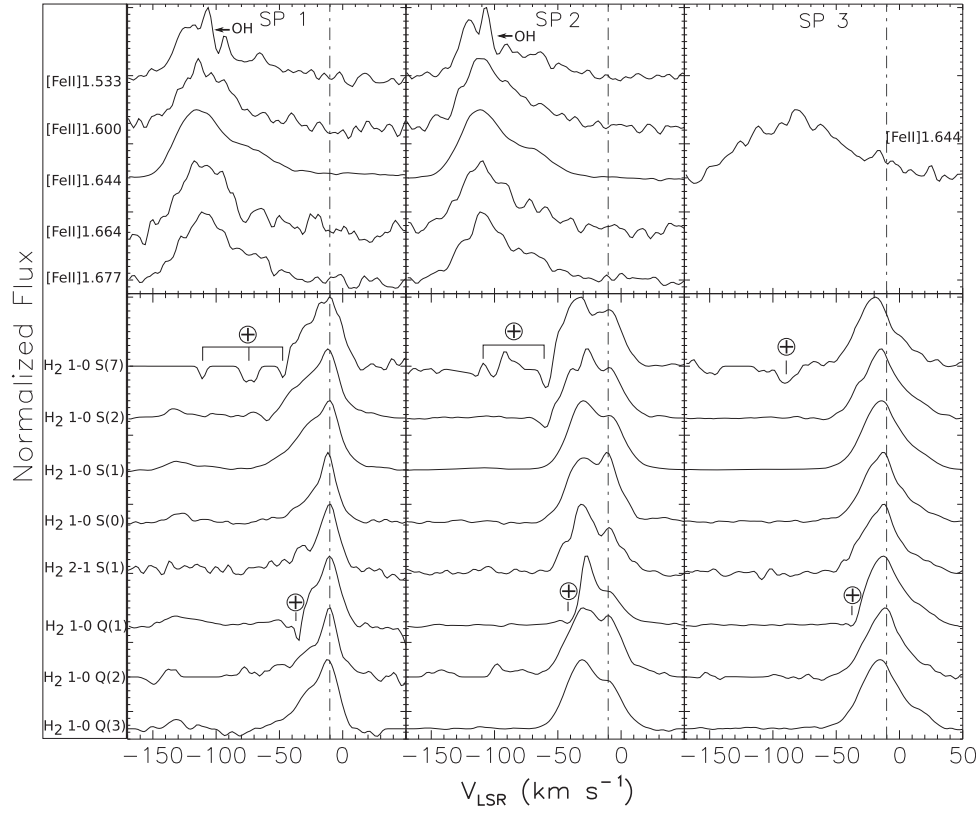
Figure 2. Line profiles of [Fe II] and H_2 toward knot A at SP 1, 2, and 3. The fluxes are integrated over $-6''.5 < Y < -0''.5$. The upper three panels show the [Fe II] $\lambda1.533$ μm, $\lambda1.600$ μm, $\lambda1.644$ μm, $\lambda1.664$ μm, and $\lambda1.677$ μm lines. The bottom three panels show H_2 $1-0$ S(7) $\lambda1.748$ μm, $1-0$ S(2) $\lambda2.034$ μm, $1-0$ S(1) $\lambda2.122$ μm, $1-0$ S(0) $\lambda2.223$ μm, $2-1$ S(1) $\lambda2.247$ μm, $1-0$ Q(1) $\lambda2.407$ μm, $1-0$ Q(2) $\lambda2.413$ μm, and $1-0$ Q(3) $\lambda2.424$ μm lines. In each line, the flux is normalized to its peak value, and the profile is smoothed by Gaussian filtering with $\sigma = 1$ pixel. In the [Fe II] $\lambda1.533$ μm line profiles, we marked the locations where the line profiles were affected by the residual after OH sky subtraction. The "$\oplus$" symbols indicate the telluric absorption features. The systemic velocity at $V_{LSR} = -10.2$ km s^{-1} (Liu et al. 2011) is indicated with dash–dotted lines.
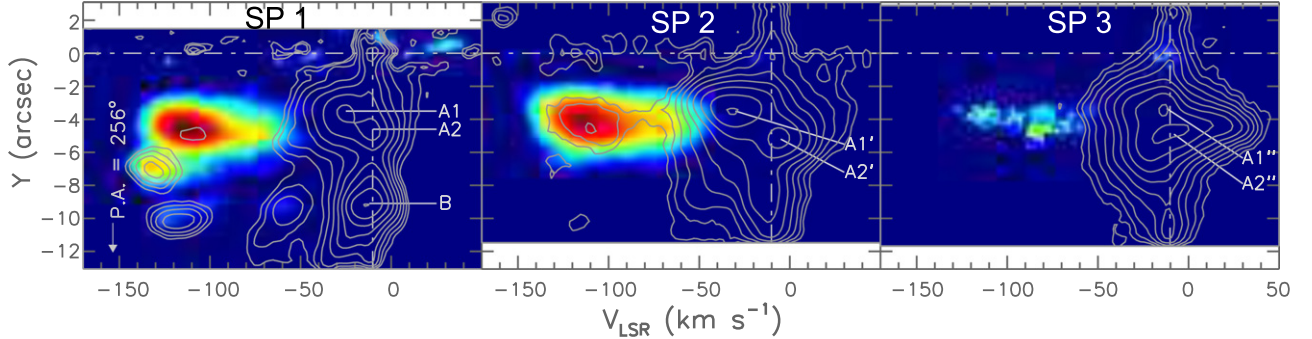
**Figure 3.** PVDs of emission from H_2 $1-0$ S(1) $\lambda2.122$ μm (white contours) and [Fe II] $\lambda1.644$ μm (color intensity map). The left, center, and right panels correspond to slit positions (SP) 1, 2, and 3, respectively. The contour starts from a 5σ level ($1\sigma = 0.02 \times 10^{-18}$ W m^{-2} Å^{-1}), and it increases with equal intervals on a logarithmic scale. In each panel, the highest contour level corresponds to 2.6, 7.7, and 3.1×10^{-18} W m^{-2} Å^{-1} (left to right). Continuum emission of LkHα 234 is removed from SP 1 and 2. The horizontal and vertical dash–dotted lines indicate $Y = 0''$ and systemic velocity ($V_{LSR} = -10.2$ km s^{-1}), respectively. SP 1 and 2 cover knots A and B, and SP 3 only includes knot A (see Figure 1(c)). Knot A shows multiple peak positions, thus we marked it as "A1" and "A2" in SP 1, "A1'" and "A2'" in SP 2, and "A1''" and "A2''" in SP 3. Knot B is marked as "B" in SP 1. Northeast is up and southwest is down in the diagrams.

At $Y \sim -6''.8$, both H_2 and [Fe II] emission show peaks at -130 km s^{-1}, which is the highest velocity in the PVD. The position of this fast peak is located on the boundary region between knot A and knot B. We detected no counter component of low velocity in the H_2 emission.

Knot B reveals three different velocity peaks in H_2 emission. They show an increase in $|Y|$ with larger $|v_{peak}|$ values. Their positions are $Y = -9''.2$, $-9''.4$, and $-10''.2$, and v_{peak} are -13, -57, and -118 km s^{-1}, respectively. All three peaks have the same, narrow velocity widths of $\sim23 \pm 1$ km s^{-1}. The lowest

velocity emission at -13 km s^{-1}, which is close to the systemic velocity, is eight times and six times brighter than those of the -57 and -118 km s^{-1} peaks, respectively.

In [Fe II], two weak peaks are detected at $Y = -9''.4$ and $-9''.9$ with v_{peak} of -59 and -120 km s^{-1}. The v_{FWHM} is wider (47 km s^{-1}) in its higher velocity peak than the slower peak (24 km s^{-1}). The positions and velocities of these peaks are consistent with -57 and -118 km s^{-1} peaks in H_2 emission. No [Fe II] emission corresponds to the position of the -13 km s^{-1} peak in H_2.
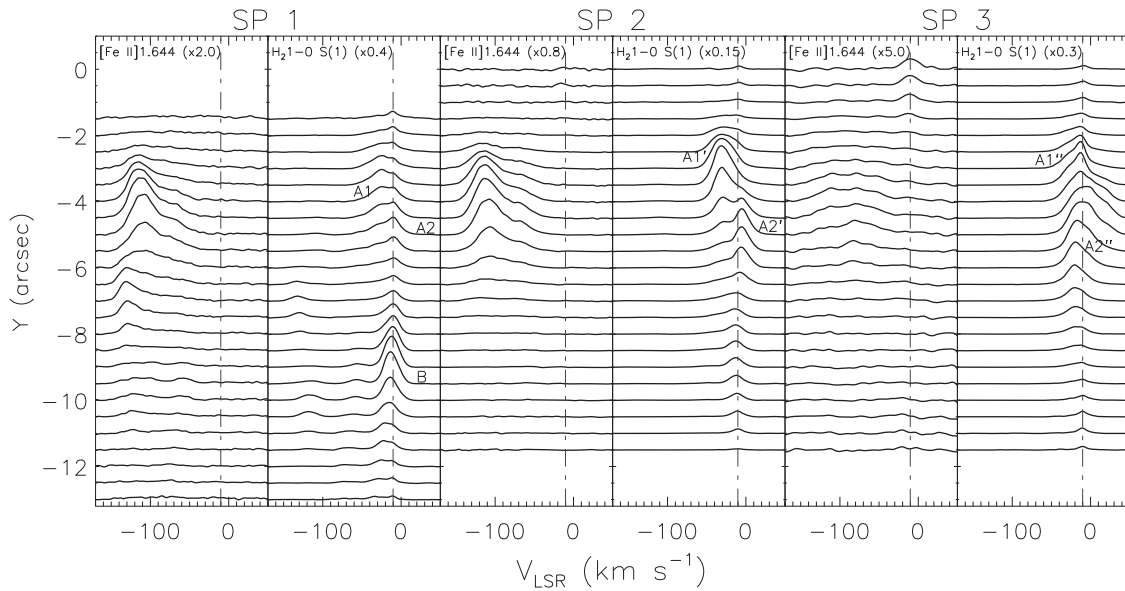
Figure 4. Line profiles of [Fe II] $\lambda1.644\ \mu m$ and H_2 1−0 S(1) $\lambda2.122\ \mu m$ lines in SP 1, 2, and 3. Line profiles are shown at every $0\rlap{.}''5$ interval in the Y direction. The peak names indicated in Figure 3 are marked. The intensity levels are amplified by factors of 2.0, 0.8, and 5.0 for [Fe II] emission, and 0.4, 0.15, and 0.3 for H_2 emission, respectively. The systemic velocity of $V_{LSR} = -10.2\ km\ s^{-1}$ is indicated with dash–dotted lines.

The [Fe II] emission usually arises from a similar shock region to the optical [S II] emission (Hamann et al. 1994). The spectroscopy of [S II] $\lambda\lambda6716$, 6731 Å in Ray et al. (1990) showed V_{LSR} of −79 and −89 km s^{-1} for knots A and B (velocities are converted from their heliocentric velocity). The peak velocities obtained from our [Fe II] observations are different from [S II]. Knot A shows ~ -113 km s^{-1} and knot B is detected at multiple velocities of −59 and −120 km s^{-1}. Although the intensity of knot B in [S II] is comparable to that of knot A, [Fe II] in knot B is about six times weaker than in knot A. One similarity between [S II] and [Fe II] spectra is that both show no emission at the systemic velocity.

The differences between H_2 1−0 S(1) $\lambda2.122\ \mu m$ and [Fe II] $\lambda1.644\ \mu m$ emission and their discrete multiple peaks will be discussed in detail in Section 4.

3.2.2. Slit Position 2 (SP 2)

SP 2 lies $\sim1\rlap{.}''2$ northwest of SP 1 (Figure 1). This position includes the central region of knot A in H_2 emission. The H_2 and [Fe II] emission in this position are strongest among the three slit positions. SP 2 grazes knot B at $Y < -6\rlap{.}''8$.

In H_2 emission, knot A shows multiple velocity peaks at $Y = -3\rlap{.}''5$ and $-5\rlap{.}''2$ with $v_{peak} \sim -30$ and -5 km s^{-1} (Figure 3). Since their positions are different from A1 and A2 in SP 1, we marked them as A1′ and A2′. The v_{peak} of A1′ is slightly faster than A1, and A2′ is redshifted compared to the systemic velocity. The velocity widths of A1′ and A2′ (~34 and ~25 km s^{-1}) are similar to those of A1 and A2, within an error range of ±3 km s^{-1}. Weak emission at a high velocity of −110 km s^{-1} is also detected at $-4\rlap{.}''7$. It is noticeable that the redshifted H_2 emission ($V_{LSR} > -10.2$ km s^{-1}) from knot A is extended to $\sim +30$ km s^{-1}.

The [Fe II] emission from knot A is similar to that of SP 1 in velocity, showing two velocity peaks. It shows a high-velocity peak of −112 km s^{-1} at $Y = -4\rlap{.}''3$ and an extended line profile toward lower velocity. The peak of the extended component shows a v_{peak} of −78 km s^{-1} and is ~2.5 times weaker than the high-velocity peak. Their velocity widths estimated from a

multiple-Gaussian fitting are ~32 and 46 km s^{-1}, respectively. The FWZI of this [Fe II] emission is the same as that of SP 1 (~130 km s^{-1}). The [Fe II] peak in SP 2 is $+0\rlap{.}''4$ in Y from the corresponding peak in SP 1. This may be caused by the different P.A. of the [Fe II] outflow and our slits.

Weak H_2 emission ($\sigma \sim 5$) is detected at $Y = -6\rlap{.}''8$ and $V_{LSR} = -130$ km s^{-1}, which coincides in the position and velocity with the highest velocity peak of H_2 and [Fe II] at SP 1.

At $Y < -6\rlap{.}''8$, a part of knot B shows a similar shape to that of SP 1 in H_2 emission: strong around the systemic velocity, high-velocity peaks and a blueshifted wing. However, there is no relevant peak feature around the systemic velocity. [Fe II] emission is not detected in knot B.

3.2.3. Slit Position 3 (SP 3)

At this position, we obtain a spectrum of the northwest part of knot A, while the slit does not cover any of the emission from knot B (Figure 1). Knot A shows two peaks, as in the previous two slit positions. Both peaks lie near the systemic velocity and we mark them as A1″ and A2″. A1″ peaks at $Y = -3\rlap{.}''35$ and shows a less negative peak velocity (−12 km s^{-1}) than A1 and A1′, with a velocity width of 36 km s^{-1}. A2″ shows multiple velocities with peaks at −5 and −13 km s^{-1} at $Y \sim -5\rlap{.}''0$. The velocity widths of the two peaks are 23 km s^{-1} and ~41km s^{-1}, respectively. In SP 3, an extension of a redshifted component at knot A in the H_2 emission is more noticeable than in SP 2. It is most extended at $Y = -4\rlap{.}''5$ and the velocity reaches over $+40$ km s^{-1}.

[Fe II] emission in SP 3 is much weaker than in SP 1 and 2, by factors of ~10 and ~25, respectively.

3.3. [Fe II] Line Ratios

Figure 5 shows the PVDs of all detected [Fe II] emission from SP 1, SP 2, and SP 3. It includes the $\lambda1.533$, $\lambda1.600$, $\lambda1.644$, $\lambda1.664$, and $\lambda1.677\ \mu m$ lines. All five lines are detected at SP 1 and 2, while SP 3 only shows emission in the $\lambda1.644$ line. In SP 1 and 2, the morphologies and velocities are
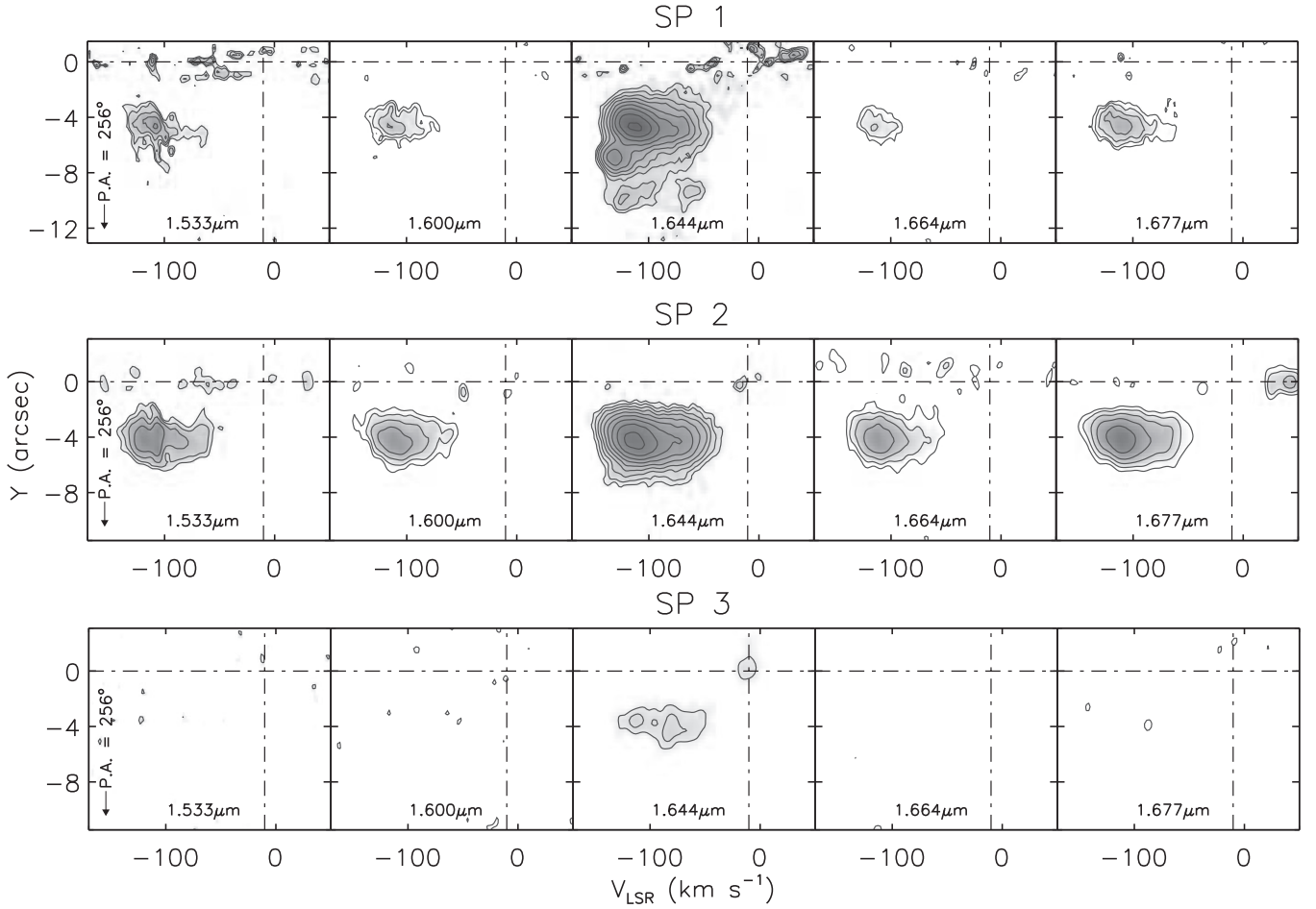
Figure 5. PVDs of [Fe II] lines obtained from SP 1 (top), SP 2 (middle), and SP 3 (bottom). Contours starts from the 4σ level and increase in equal intervals on a logarithmic scale. The highest contours in 1.644 μm indicate 0.6, 1.3, and 0.1 $\times$ 10^{-18} W m^{-2} Å^{-1} in SP 1, SP 2, and SP 3 respectively. In 1.533 and 1.600 μm, sky OH emission caused the absorption/emission features at ~ -120 km s^{-1}. A dash–dotted horizontal line indicates the position $Y = 0''$. The systemic velocity is indicated with a dash–dotted vertical line in each panel.

almost the same in all of the lines in each slit position. One exception is in SP 1, where the highest velocity peak at $V_{\mathrm{LSR}} \sim -130$ km s^{-1}, $Y = -6''8$ and weak emission at $Y = -9''4$ and $-9''9$ are only detected in $\lambda1.644$ μm. Measured line fluxes normalized to the [Fe II] $\lambda1.644$ μm line are listed in Table 1. Since the positions and velocities of peaks in all [Fe II] lines are consistent, the fluxes are estimated within the regions at $Y \sim 4''7 \pm 0''4$, $V_{\mathrm{LSR}} \sim -113 \pm 10$ km s^{-1} and at $Y \sim 4''3 \pm 0''4$, $V_{\mathrm{LSR}} \sim -112 \pm 10$ km s^{-1} in SP 1 and SP 2, respectively. The line fluxes in SP 1 and SP 2 are very similar.

Near-IR [Fe II] emission lines can be used as effective tracers of electron density (n_{e}) in stellar outflows (Nisini et al. 2002; Pesenti et al. 2003; Takami et al. 2006). Nisini et al. (2002) developed a non-LTE model applicable to jets from YSOs, considering the first 16 fine structure levels of the Fe^{+} ion. The flux ratios between lines obtained in our observations are relatively independent of gas temperature, because the lines are all from the fine structure level of the a^4D term, having excitation energies in the range of 10,000–12,000 K (Nisini et al. 2002). To investigate the electron density, we show the line ratios superposed on the model grids from Nisini et al. (2002) in Figure 6. In SP 1 and 2, the electron densities (log n_{e}) averaged from the three ratios of $\lambda1.600$, $\lambda1.533$, and $\lambda1.677$ μm lines against the $\lambda1.644$ μm line are $4.0^{+0.7}_{-0.6}$ and $4.1^{+0.9}_{-0.6}$, respectively. The uncertainty in the $\lambda1.644$ μm/

Table 1
[Fe II] Line Fluxes Normalized to the 1.644 μm Flux

Line	$\lambda(\mu m)$	SP 1	SP 2
$a^4D_{5/2} - a^4F_{9/2}$	1.53389	0.12 ± 0.05	0.14 ± 0.06
$a^4D_{3/2} - a^4F_{7/2}$	1.59991	0.10 ± 0.04	0.11 ± 0.04
$a^4D_{7/2} - a^4F_{9/2}$	1.64400	1.00 ± 0.29	1.00 ± 0.18
$a^4D_{1/2} - a^4F_{5/2}$	1.66422	0.09 ± 0.03	0.10 ± 0.04
$a^4D_{5/2} - a^4F_{7/2}$	1.67733	0.17 ± 0.04	0.18 ± 0.06

Note. The reddening is not corrected.

$\lambda1.533$ μm ratio is larger (Figure 6), due to residuals after a subtraction of the OH sky emission in the $\lambda1.533$ μm line. The n_{e} of knot A we obtained from the optical [S II] doublet ratio (Osterbrock 1989) is about 0.3×10^4 cm^{-3}, which is smaller than that estimated from near-IR ion emission lines here. This result is consistent with the tendency in Nisini et al. (2002). It indicates that the [Fe II] lines are able to probe a denser region in the jet because they have a higher critical density ($\sim10^4$ cm^{-3}) than that of the [S II] ($\sim10^3$ cm^{-3}).

The electron densities of 0.5–3.2×10^4 cm^{-3} obtained here are similar to or smaller than those estimated from [Fe II] emission from T Tauri stars and intermediate-mass stars in
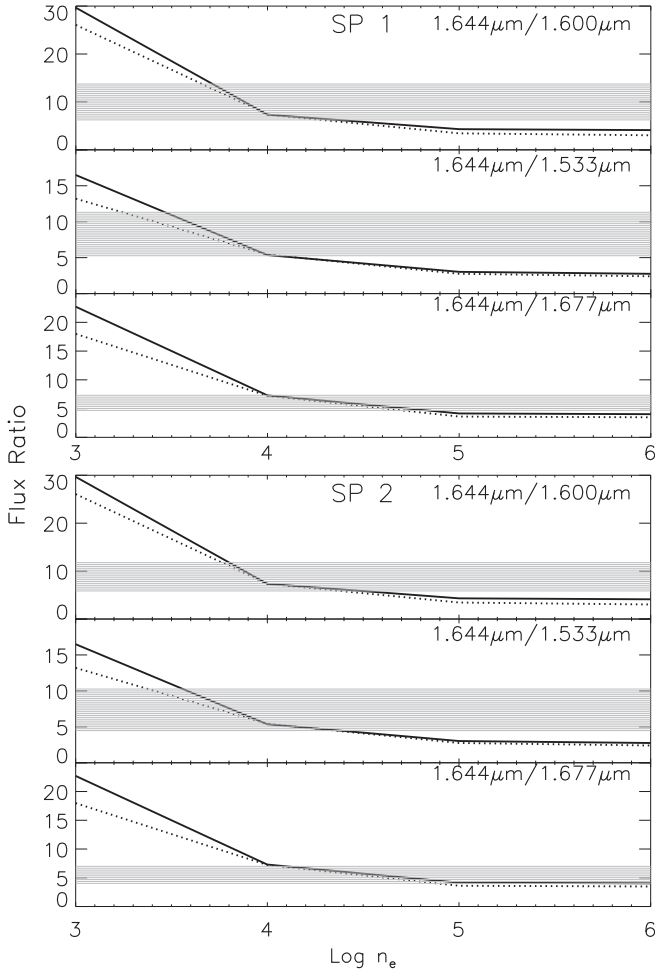
Figure 6. The observed flux ratios of [Fe II] $\lambda1.644$ μm/$\lambda1.600$ μm, $\lambda1.644$ μm/$\lambda1.533$ μm, and $\lambda1.644$ μm/$\lambda1.677$ μm in SP 1 (top three panels) and SP 2 (bottom three panels) superposed on the electron density (n_e) model from Nisini et al. (2002). Solid and dotted lines represent excitation temperatures of 4,000 K and 15,000 K in the model, respectively. The areas shaded gray correspond to observed flux ratios including uncertainties.

Hamann et al. (1994). In addition, these are also slightly lower than values from HH outflows from Class 0−I, which range from 10^4 to 10^5 cm^{-3} (Nisini et al. 2002; Takami et al. 2006).

3.4. H$_2$ Line Ratios

Table 2 lists the line fluxes of all 14 emission lines detected in these observations. Fluxes are estimated at each peak position in Figure 3, and normalized to the H$_2$ 1−0 S(1) $\lambda2.122$ μm line. Figure 7 shows the PVDs of eight selected H$_2$ emission lines. In all slit positions, the different H$_2$ emission lines show similar velocity features, as different [Fe II] lines do. In all H$_2$ lines at SP 1, 2, and 3, we detected emission from both knot A and knot B, which are bright at low velocity. The three high-velocity components at $Y = -6\farcs8$, $-9\farcs4$, and $-10\farcs2$ with v_{peak} of -130, -13, and -118 km s^{-1} shown in $\lambda2.122$ μm are also detected in $\lambda2.034$, $\lambda2.223$, $\lambda2.407$, and $\lambda2.424$ μm lines. In $\lambda2.407$ μm at SP 2, we detected a weak (5σ level) emission that is consistent with a peak at $Y = -4\farcs7$ with -110 km s^{-1} in $\lambda2.122$ μm.

Figure 8 shows H$_2$ population diagrams calculated from the fluxes in Table 2. The level populations of hydrogen molecular gas estimated from ro-vibrational transitions allow us to study the excitation state and temperature of the gas (Black & Dalgarno 1976; Gautier et al. 1976; Beckwith et al. 1978; Hasegawa et al. 1987). We calculated the upper-level column density from the observed line flux after a reddening correction. The extinction can be estimated using the ratios of the emission lines originating from the same upper levels. In our calculation, we used the ratios of three pairs of 1−0 S(1)/1−0 Q(3), 1−0 S(0)/1−0 Q(2), and 1−0 S(2)/1−0 Q(4). We adopted the transition probabilities from Turner et al. (1977). We apply the extinction law, $A_\lambda = A_V(0.55\mu m/\lambda)^{1.6}$ (Rieke & Lebofsky 1985). In our estimation, A_H and A_K are very small (<0.1). We used $A_V = 3.4$, which is an intermediate from the range of 3.1–5.1 used in previous studies (Hillenbrand et al. 1992; Hernández et al. 2004; Liu et al. 2011).

For the data in Figure 8, we applied weighted least-squares fitting to estimate rotational temperatures (T_{rot}) from an upper level of $v = 1$ (circle) and $v = 2$ (square), considering $1/\sigma^2$ for weights, where σ is the uncertainty in the level population. We excluded one transition from $v = 3$ (triangle) from the fit due to its large uncertainty. Solid and dashed lines represent the fitting lines for $v = 1$ and 2, respectively.

In SP 1, T_{rot} of all peaks estimated in $v = 1$ is 2500 ± 200 K. The temperatures in $v = 2$ show uncertainty because we have only three data points for the fitting. T_{rot} of peaks A1 and B in $v = 2$ are similar, 3200 ± 1500 K. In A2, T_{rot} in $v = 2$ is 2500 ± 1100 K, which is close to the value from $v = 1$. In SP 2, T_{rot} in A1′ is almost the same as in A1, in both $v = 1$ and 2. Peak A2′ shows a higher T_{rot} than A2 in $v = 1$ and 2, but the differences are within the uncertainties. In SP 3, T_{rot} from A1″ and A2″ in $v = 1$ are higher than those of SP 1 and 2; with $T_{rot} > 2700 \pm 250$ K. In $v = 2$, T_{rot} is 3000 ± 1500 K for both A1″ and A2″. From SP 1 to 3, T_{rot} in $v = 1$ shows a small increase, but within uncertainties. For $v = 2$, there is no clear trend with change in slit position. In all three slit positions, in both $v = 1$ and 2 the derived T_{rot} is ~2500–3000 K. This means that the gases are thermalized at a single ro-vibrational temperature, because both level populations follow the same T_{rot}. We note that the temperature estimation differs when we consider different A_V in the flux correction. It becomes ~200 K lower and less than 100 K higher for the cases of $A_V = 0$ and 5.1, respectively, compared to the estimation using $A_V = 3.4$. We also note that the populations of ortho and para transitions are aligned in a single line. This indicates that the emission lines are not from the fluorescent H$_2$ by UV excitation (e.g., Hasegawa et al. 1987).

Thermalization has been observed in the shocked gas in the outflows from low- and high-mass stars (e.g., HH 111, HH 240 and 241 in Nisini et al. 2002, Orion KL peak1 in Beckwith et al. 1983). We can test the properties of a shock with a population diagram by comparison with model data. Rosenthal et al. (2000) have investigated various shock models to prove a shock nature in Orion Peak 1, and they showed that the combining of shock models could explain their observational results except at the highest excitation level. Since we assume the presence of a bow shock in this region (see Section 4), we plotted the bow shock model with $v_{shock} = 100$ km s^{-1} from Smith (1991) in Figure 8 (dotted lines). This model is more consistent with fitting lines from $v = 2$ than those from $v = 1$. On the other hand, it is hard to discriminate the type of shock from our result because there is no significant difference between various shock models in the energy levels of 0.5–2 $\times 10^4$ K (Rosenthal et al. 2000).

Table 2
H$_2$ Line Fluxes Normalized to the 1−0 S(1) Flux

Line	$\lambda(\mu m)$	SP 1			SP 2		SP 3	
		A1	A2	B	A1′	A2′	A1″	A2″
1−0 S(9)	1.68772	0.02 ± 0.01	0.02 ± 0.01	0.02 ± 0.01	0.02 ± 0.01	0.02 ± 0.01	0.02 ± 0.01	0.02 ± 0.01
1−0 S(7)	1.74803	0.04 ± 0.02	0.04 ± 0.02	0.05 ± 0.01	0.02 ± 0.01	0.02 ± 0.01	0.02 ± 0.01	0.02 ± 0.02
1−0 S(6)	1.78795	0.02 ± 0.01	0.02 ± 0.01	0.02 ± 0.01	0.02 ± 0.01	0.03 ± 0.01	0.03 ± 0.02	0.03 ± 0.02
1−0 S(2)	2.03376	0.19 ± 0.04	0.19 ± 0.04	0.19 ± 0.02	0.21 ± 0.03	0.23 ± 0.04	0.23 ± 0.06	0.22 ± 0.05
2−1 S(3)	2.07351	0.07 ± 0.04	0.07 ± 0.04	0.09 ± 0.01	0.08 ± 0.02	0.07 ± 0.03	0.09 ± 0.03	0.06 ± 0.03
1−0 S(1)	2.12183	1.00 ± 0.14	1.00 ± 0.13	1.00 ± 0.05	1.00 ± 0.14	1.00 ± 0.14	1.00 ± 0.14	1.00 ± 0.15
2−1 S(2)	2.15423	0.04 ± 0.02	0.06 ± 0.02	0.04 ± 0.01	0.03 ± 0.01	0.03 ± 0.01	0.05 ± 0.02	0.03 ± 0.02
3−2 S(3)	2.20139	0.01 ± 0.01	0.02 ± 0.01	0.02 ± 0.01	0.02 ± 0.01	0.02 ± 0.01	0.03 ± 0.02	0.02 ± 0.02
1−0 S(0)	2.22329	0.23 ± 0.05	0.22 ± 0.05	0.24 ± 0.02	0.19 ± 0.03	0.20 ± 0.04	0.22 ± 0.05	0.21 ± 0.05
2−1 S(1)	2.24771	0.08 ± 0.02	0.11 ± 0.03	0.10 ± 0.01	0.08 ± 0.02	0.06 ± 0.02	0.09 ± 0.03	0.06 ± 0.03
1−0 Q(1)	2.40659	0.40 ± 0.08	0.47 ± 0.08	0.47 ± 0.03	0.37 ± 0.06	0.32 ± 0.06	0.37 ± 0.07	0.37 ± 0.07
1−0 Q(2)	2.41344	0.14 ± 0.04	0.15 ± 0.04	0.14 ± 0.02	0.12 ± 0.03	0.11 ± 0.03	0.13 ± 0.04	0.11 ± 0.04
1−0 Q(3)	2.42373	0.27 ± 0.06	0.24 ± 0.05	0.25 ± 0.02	0.20 ± 0.03	0.18 ± 0.04	0.22 ± 0.05	0.19 ± 0.05
1−0 Q(4)	2.43749	0.08 ± 0.01	0.09 ± 0.01	0.07 ± 0.01	0.06 ± 0.01	0.05 ± 0.01	0.07 ± 0.03	0.06 ± 0.03

Note. The reddening is not corrected.

In Table 3, we list the H$_2$ line ratios at all peak positions that are sensitive to the type of shock. The ratios in the models of C- and J-type shocks and UV pumping are taken from Beck et al. (2008). The ratios in our observation are similar to those of outflows from T Tauri stars (Beck et al. 2008). The 2−1 S(1)/1 −0 S(1) ratio is close to a C-type shock in all cases, indicating similar shock conditions along the outflow. The other three ratios do not help discriminate between different shocks, because of the large uncertainties. There are no significant differences at all three slit positions. We note that the 1−0 S (1)/1−0 Q(1) ratios in our data are about 1.5–2.5 times higher than ratios from all models. 1−0 Q(1) $\lambda2.407\,\mu m$ emission is affected by a deep telluric absorption at $\sim -40\,km\,s^{-1}$ ("$\oplus$" symbols in Figure 7), so it may not be reliable.

4. DISCUSSION

4.1. [Fe II] and H$_2$ Emission

As shown in Section 3, the H$_2$ 1−0 S(1) $\lambda2.122\,\mu m$ and [Fe II] $\lambda1.644\,\mu m$ emission lines have very different velocity structures. The H$_2$ emission is dominant at low velocity while [Fe II] emission dominates at high velocity. This trend was found in outflows from both classical T Tauri stars and Class 0 −I YSOs (e.g., Pyo et al. 2002; Davis et al. 2003; Takami et al. 2006). The trend makes sense in the context of an interpretation where the shocked H$_2$ emission arises from gas entrained by a high-velocity outflow (Pyo et al. 2002).

In our PVDs, we detected H$_2$ emission at the systemic velocity along the whole slit, in all three slit positions. This emission probably originates from ambient molecular hydrogen gas in this region, which corresponds to the presence of far-UV radiation by producing a photodissociation region (PDR) (Morris et al. 2004). However, taking account of the H$_2$ lines ratios (Table 3), we should not rule out excitation by shock as the emission source. We note that, in this case, the velocity width at the top of the PVDs should be larger than the current value ($\sim10\,km\,s^{-1}$), because the angle of the outflow axis may be less than 45° with respect to the line of sight according to our interpretation in bow shock features described below.

Discrete multiple velocity components revealed from the H$_2$ emission in Figure 3 are the typical high- and low-velocity features that arise from the bow shock in outflows (Hartigan et al. 1987; Davis et al. 2003; O'Connell et al. 2004). If the inclination angle between the axis of the bow shock and the line of sight is in a range of $\sim0°$–45°, the emissions from the apex and the wing of the bow are seen as separate high- and low-velocity peaks. The weak H$_2$ and strong [Fe II] emissions at high velocity ($V_{LSR} \sim -120\,km\,s^{-1}$) show good agreement in position and velocity, indicating that the [Fe II] emission lines usually arise from the bow apex, where the jet is faster than the surrounding region (Hartigan et al. 1987; Davis et al. 2003). The velocity difference of $\sim100\,km\,s^{-1}$ between the high- and low-velocity peaks in the H$_2$ lines is similar to that observed in the jet of L1551-IRS 5 (Davis et al. 2003), which has an inclination angle of $\sim 45°$ with respect to the line of sight. In knot B at SP 1, we see three discrete velocity peaks in H$_2$ where the velocity of the peak increases with increasing $|Y|$. The more blueshifted peaks lie farther from the star. The total offset along the outflow is $\sim1\rlap{.}''15$, after consideration of the different angles of our slit (256°) and the outflow axis (227°). One possible interpretation of this position shift is a spatial difference between the faster gas in the bow apex and the slower portion in the bow wing. We cannot rule out, however, the possibility that this shift is caused by distinct knots originally located at different positions.

In contrast to the blueshifted gas seen at all slit positions, the redshifted component ($V_{LSR} > -10.2\,km\,s^{-1}$) seen in H$_2$ at SP 2 and 3 seems to arise from another, spatially unresolved outflow. Since the slit positions are pointing at the blue lobe of the jet (see Sections 1 and 2), at locations where the blueshifted material is well separated in phase space from any ambient emission, the detection of redshifted emission implies the existence of a distinct outflow, separated from the high-velocity blueshifted jet. This outflow may have an axis almost parallel to the plane of the sky, with a wide outflow opening angle, because it shows both blue and redshifted components at low velocity ($-50\,km\,s^{-1} < V_{LSR} < +50\,km\,s^{-1}$). For a further discussion, we need additional clues to the position and orientation of the redshifted component, which would need to come from further observations with high spectral resolution and with higher spatial resolution than we can obtain with our present instrument/telescope combination.
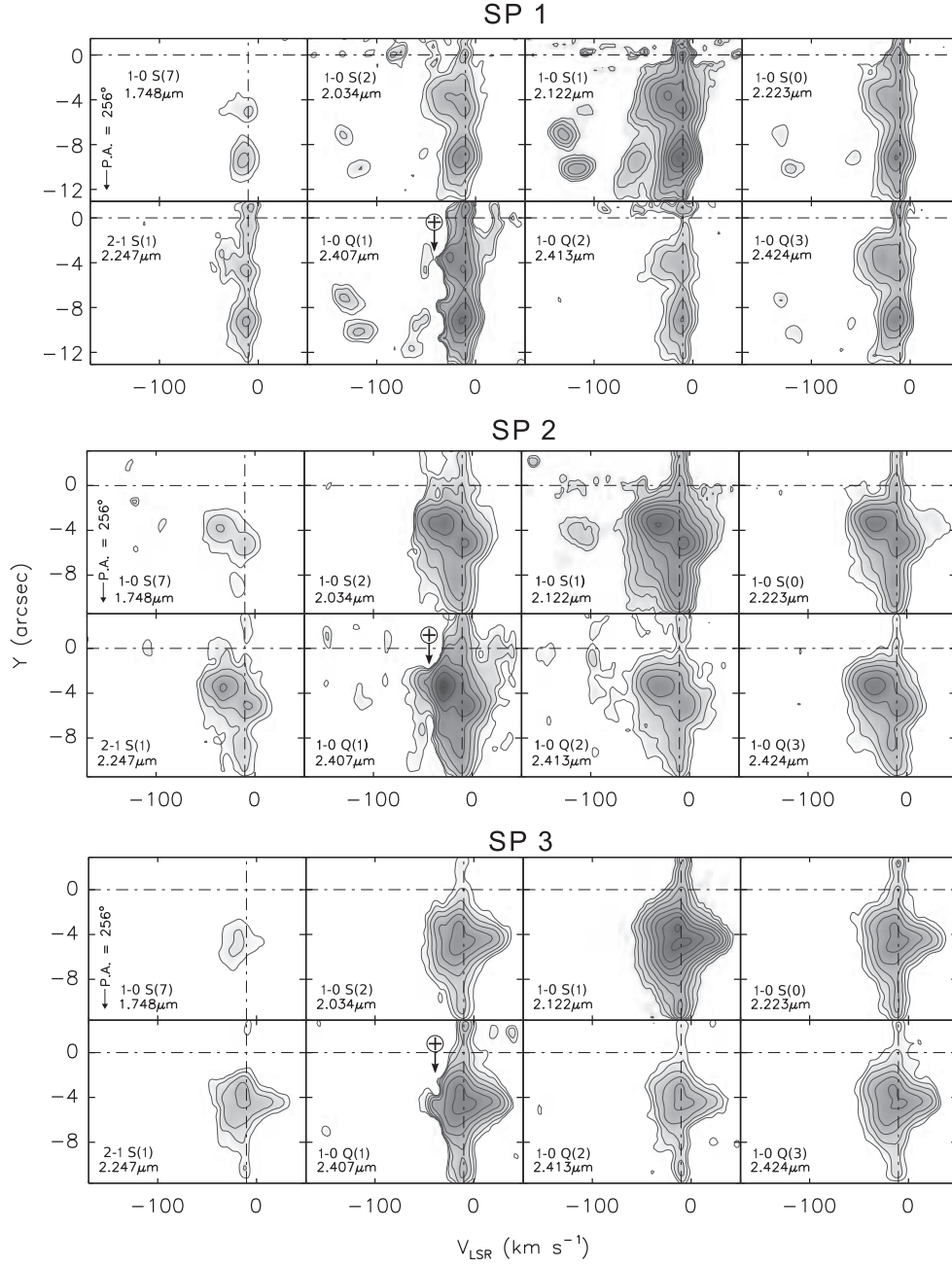
Figure 7. PVDs of H_2 lines from SP 1 (top), SP 2 (middle), and SP 3 (bottom). The continuum emission from LkHα 234 is subtracted in SP 1 and SP 2. The residuals from the subtraction are shown at $Y = 0 \pm 2''$. Contours start from the 4σ level and increase in equal intervals on a logarithmic scale. The highest contour levels in 2.122 μm correspond to 2.6, 7.7, and 3.1 $\times 10^{-18}$ W m^{-2} Å^{-1} for SP 1, 2, and 3. The "$\oplus$" symbols at -40 km s^{-1} in 2.407 μm of all slit positions indicate the deep atmospheric absorption. Dash–dotted horizontal lines indicate the $Y = 0''$ position. The systemic velocity is shown with a dash–dotted vertical line in each panel.

4.2. Driving Sources of Multiple Outflows

As shown in Section 1 and Figure 1, the LkHα 234 region is complicated with several outflow sources observed at mid-IR, millimeter, and radio wavelengths. In this section, we summarize three separate outflows and their source candidates, and relate them to our own spectroscopic observations.

1. The [Fe II] jet from VLA 3 (NW 1, IRS 6): At SP 1 and 2, we detected the bright [Fe II] emission with a velocity of ~ -120 km s^{-1} at the position of knot A (Figure 3). Here, we suggest that this [Fe II] emission possibly originates from the outflow driven by radio source VLA 3B, according to following evidence.

The PVDs at SP 1 and 2 show that the [Fe II] knot lies between $Y = -2''$ and $Y = -6''$. As shown in Figure 1, its position agrees well with the "green blob" feature seen in the center of the C-shaped reflection nebula in the *JHK* color image of Kato et al. (2011), a feature that is probably caused by [Fe II] emission in the *H*-band. The narrow-band [Fe II] $\lambda 1.644$ μm image in Schultz et al. (1995), which showed emission at the same position, supports this conclusion. The configuration of an [Fe II] jet detected along the central axis of a cavity in a reflection nebula is very similar to the case of L1551-IRS 5 (Hayashi & Pyo 2009). Kato et al. (2011) showed two jet-like features in their *J*- and *H*-band images and they mentioned that those features point at YSO candidate G. They suggested that
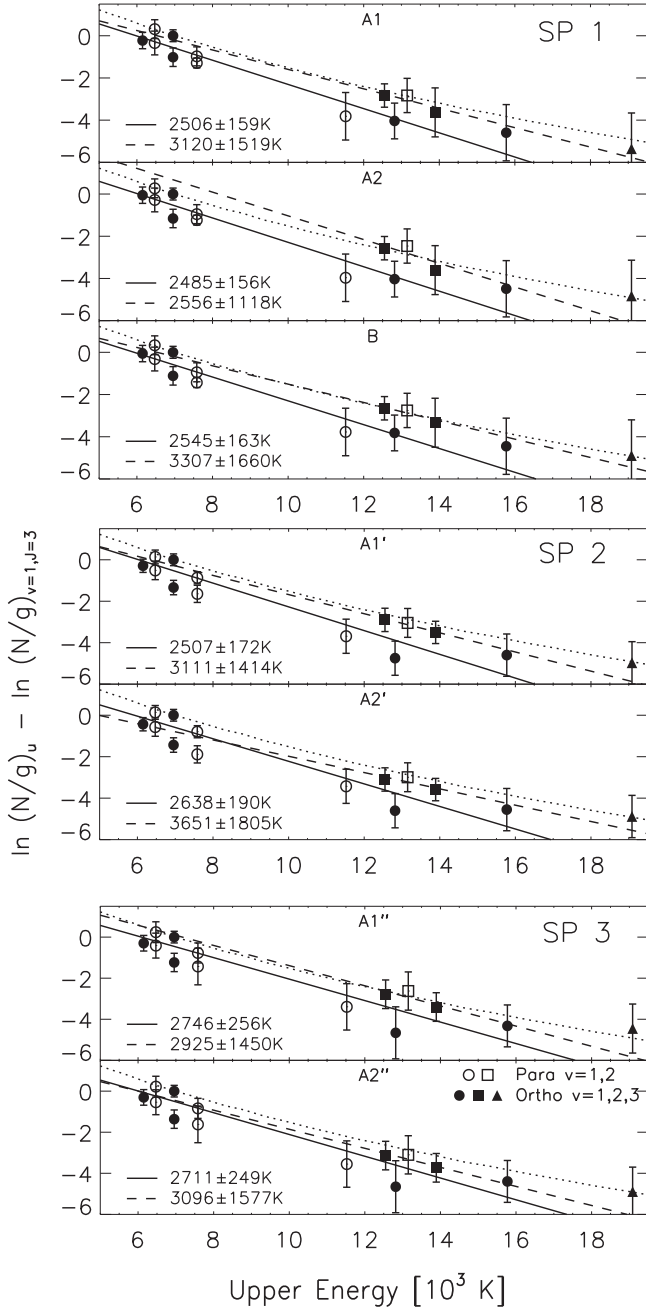
Figure 8. The level population diagrams of H_2 for knots A1, A2, and B of SP 1 (top), A1$'$ and A2$'$ of SP 2 (middle), and A1$''$ and A2$''$ of SP 3 (bottom). Open and filled symbols indicate ortho and para transitions, respectively. Circles, squares, and triangles correspond to the upper vibrational levels of 1, 2, and 3 respectively. Solid and dashed lines are fitting lines for the vibrational levels of 1 and 2 from a weighted least-squares regression, respectively. Dotted lines represent the population ratio of the bow shock model (Smith 1991). The excitation temperatures measured from the slopes of the lines are indicated in the lower left of each panel. $A_V = 3.4$ is used for reddening correction, and the values are normalized to the 1−0 S(1) transition.

the jet-like feature containing the green blob is associated with the optical [S II] jet.

We suggest another possible origin of the [Fe II] emission in Figure 3, VLA 3B. The 3.6 cm continuum map of Trinidad et al. (2004) showed that VLA 3B has an elongated thermal radio jet extending northeast–southwest. Their source-subtracted 3.6 cm map is shown in Figure 1(d). We estimated a P.A. of ~230° for this jet. "Axis3" in Figure 1 denotes the axis

of the radio jet in VLA 3B. This line passes through the positions of the [Fe II] knot detected in our observations and the green blob in the *JHK* image. The very similar major-axis position angles of the [Fe II] emission in Schultz et al. (1995) and the radio thermal jet also support our suggestion, although the reliability of their [Fe II] image close to LkHα 234 should be a cause for caution. Taking all factors into account, however, we conclude that this [Fe II] emission is from a jet driven by VLA 3B, with a velocity of $V_{LSR} \sim -120\ km\ s^{-1}$. Trinidad et al. (2004) suggested that VLA 3B could be a low-mass YSO, while Kato et al. (2011) suggested NW 1 as a B6–B7-type YSO from the spectral energy distribution. An outflow cavity is opening toward the southwest from VLA 3B. The mid-IR source IRS 6 lies in the cavity with a ~0.″5 offset from VLA 3B. The offset implies that the mid-IR emission comes from a region less affected by dust extinction.

We note that the P.A. of the [Fe II] jet is very similar to that of the H_2 jet (227°), as shown in Figure 1. This may be an additional example of multiple jets sharing a similar orientation (e.g., Nisini et al. 2001), as pointed out by Trinidad et al. (2004).

2. The H_2 jet from FIRS1-MM1: The most likely source of the H_2 jet (Cabrit et al. 1997) and inner [S II] jet (Ray et al. 1990) is FIRS1-MM1 (Fuente et al. 2001), which is indicated as a white pentagon in Figure 1. More accurately, it seems to drive knots B and C, because the position of FIRS1-MM1 is well aligned with the line through those two knots (P.A. ~227°), which is marked as "Axis2" in Figure 1. In Figure 3 at SP 1, the H_2 emission shows a peak at $Y = -9.″2$. This peak position shows that SP 1 is superposed on the center position of knot B of the H_2 jet, as we confirm in Figure 1. We used our high-resolution observation to reveal, for the first time, that knot B shows multiple velocity peaks, which imply the presence of a bow shock (see also Section 4.1).

3. The outer [S II] jet from VLA 2 (NW 2): The proper motion and the locations of H_2O masers around radio continuum VLA 2 (Trinidad et al. 2004; Marvel 2005; Torrelles et al. 2014) confirmed that VLA 2 is the most likely source of redshifted CO outflow (Mitchell & Matthews 1994; Fuente et al. 2001) and the outer [S II] jet (knot D–E in Ray et al. 1990), showing good agreement in direction. In Figure 1, the axis of the [S II] outflow is shown as "Axis1" with a P.A. of ~252°. Although SP 3 is located along the direction of the outer [S II] jet from VLA 2 at $Y \sim -2.″6$, we could not obtain information related to the outer [S II] jet because there is no detection of any significant [Fe II] emission feature along SP 3, and the slit position only covers the inner [S II] jet region (Ray et al. 1990).

5. SUMMARY

We have presented results from the first high-resolution near-IR spectroscopy toward the multiple outflows around the Herbig Be star LkHα 234.

1. We detected 14 H_2 and 5 [Fe II] emission lines in the *H*- and *K*-bands, including the H_2 1−0 S(1) λ2.122 μm and λ1.644 μm lines.

2. We newly revealed an [Fe II] jet driven by radio source VLA 3B.

3. The multiple velocity peaks we observe in H_2 emission lines are consistent with a generic bow shock model. Both knots A and B show this bow shock feature. Furthermore, the positional difference (~1″) between low- and high-velocity

Table 3
H$_2$ Line Ratios

Ratio	SP 1			SP 2		SP 3		Model		
	A1	A2	B	A1′	A2′	A1″	A2″	C-shock	J-shock	UV-pumped
2−1 S(1)/1−0 S(1)	0.08 ± 0.02	0.11 ± 0.03	0.10 ± 0.01	0.08 ± 0.02	0.06 ± 0.02	0.09 ± 0.03	0.06 ± 0.03	0.05	0.24	0.55
1−0 S(2)/1−0 S(0)	0.81 ± 0.23	0.86 ± 0.24	0.82 ± 0.10	1.07 ± 0.18	1.16 ± 0.26	1.07 ± 0.34	1.02 ± 0.34	1.56	2.08	1.09
2−1 S(1)/2−1 S(3)	1.18 ± 0.74	1.50 ± 0.93	1.05 ± 0.17	0.97 ± 0.35	0.87 ± 0.43	0.99 ± 0.47	0.97 ± 0.62	1.08	0.73	1.58
1−0 S(1)/1−0 Q(1)	2.51 ± 0.49	2.11 ± 0.36	2.12 ± 0.15	2.67 ± 0.55	3.09 ± 0.43	2.69 ± 0.51	2.71 ± 0.52	1.29	1.59	1.00

Note. The H$_2$ line ratios of C- and J-type shocks and UV-pumped cases are taken from Table 6 of Beck et al. (2008), who referred to the calculations in Smith (1995) and Black & van Dishoeck (1987).

components may be caused by a difference between the wing and apex of the bow.

4. The molecular hydrogen emission is dominant at low velocity with a radial velocity within 50 km s^{-1} of the systemic velocity, while [Fe II] emission is only present in the higher velocity ranges ($V_{LSR} \sim -100$ to -130 km s^{-1}). This trend has been observed in previous studies and may be understood from the assumption that the H_2 emission originates from shocked gas entrained by a fast outflow. We also detected narrow H_2 emission along the whole slit length at systemic velocity, which indicates the background PDR.

5. From the ratios of [Fe II] emission lines, we estimate an electron density of $\sim 1.1 \times 10^4$ cm^{-3}. This is similar to or slightly smaller than the values in outflows from T Tauri stars or Class 0−I sources.

6. The population diagrams of hydrogen molecules show that the gas is thermalized at a temperature of 2500–3000 K in this region. This indicates that the emission arises from shock-excited gas. The ratios between H_2 lines at knots A and B are close to those from C-type shock models (Smith 1995).

REFERENCES

Bae, J.-H., Kim, K.-T., Youn, S.-Y., et al. 2011, ApJS, 196, 21
Bechis, K. P., Harvey, P. M., Campbell, M. F., & Hoffmann, W. F. 1978, ApJ, 226, 439
Beck, T. L., McGregor, P. J., Takami, M., & Pyo, T.-S. 2008, ApJ, 676, 472
Beckwith, S., Evans, N. J., II, Gatley, I., Gull, G., & Russell, R. W. 1983, ApJ, 264, 152
Beckwith, S., Persson, S. E., Neugebauer, G., & Becklin, E. E. 1978, ApJ, 223, 464
Bertout, C. 1987, in IAU Symp. 122, Circumstellar Matter, ed. I. Appenzeller & C. Jordan (Dordrecht: Reidel), 122, 23
Black, J. H., & Dalgarno, A. 1976, ApJ, 203, 132
Black, J. H., & van Dishoeck, E. F. 1987, ApJ, 322, 412
Cabrit, S., Lagage, P.-O., McCaughrean, M., & Olofsson, G. 1997, A&A, 321, 523
Cesarsky, C. J., Cesarsky, D. A., Lequeux, J., & Churchwell, E. 1978, A&A, 68, 33
Connelley, M. S., Reipurth, B., & Tokunaga, A. T. 2008a, AJ, 135, 2496
Connelley, M. S., Reipurth, B., & Tokunaga, A. T. 2008b, AJ, 135, 2526
Davis, C. J., Whelan, E., Ray, T. P., & Chrysostomou, A. 2003, A&A, 397, 693
Duquennoy, A., & Mayor, M. 1991, A&A, 248, 485
Edwards, S., & Snell, R. L. 1983, ApJ, 270, 605
Eislöffel, J. 2000, A&A, 354, 236
Fuente, A., Neri, R., Martín-Pintado, J., et al. 2001, A&A, 366, 873
Gautier, T. N., III, Fink, U., Larson, H. P., & Treffers, R. R. 1976, ApJL, 207, L129
Hamann, F., Simon, M., Carr, J. S., & Prato, L. 1994, ApJ, 436, 292
Hartigan, P., Edwards, S., & Ghandour, L. 1995, ApJ, 452, 736
Hartigan, P., Raymond, J., & Hartmann, L. 1987, ApJ, 316, 323
Hasegawa, T., Gatley, I., Garden, R. P., et al. 1987, ApJL, 318, L77
Hayashi, M., & Pyo, T.-S. 2009, ApJ, 694, 582
Hernández, J., Calvet, N., Briceño, C., Hartmann, L., & Berlind, P. 2004, AJ, 127, 1682
Hillenbrand, L. A., Strom, S. E., Vrba, F. J., & Keene, J. 1992, ApJ, 397, 613
Jeong, U., Chun, M.-Y., Oh, J. S., et al. 2014, Proc. SPIE, 9154, 91541X
Kato, E., Fukagawa, M., Perrin, M. D., et al. 2011, PASJ, 63, 849
Lada, C. J., & Lada, E. A. 2003, ARA&A, 41, 57
Liu, T., Zhang, H., Qin, S.-L., et al. 2011, ApJ, 734, 22
Marvel, K. B. 2005, AJ, 130, 2732
McGroarty, F., Ray, T. P., & Bally, J. 2004, A&A, 415, 189
Mitchell, G. F., & Matthews, H. E. 1994, ApJL, 423, L55
Morris, P. W., Noriega-Crespo, A., Marleau, F. R., et al. 2004, ApJS, 154, 339
Nisini, B., Caratti o Garatti, A., Giannini, T., & Lorenzetti, D. 2002, A&A, 393, 1035
Nisini, B., Massi, F., Vitali, F., et al. 2001, A&A, 376, 553
O'Connell, B., Smith, M. D., Davis, C. J., et al. 2004, A&A, 419, 975
Oh, J. S., Park, C., Cha, S.-M., et al. 2014, JASS, 31, 177
Osterbrock, D. E. 1989, Astrophysics of Gaseous Nebulae and Active Galactic Nuclei (Research Supported by the University of California, John Simon Guggenheim Memorial Foundation, University of Minnesota, et al.; Mill Valley, CA, Univ. Science Books), 422
Park, C., Jaffe, D. T., Yuk, I.-S., et al. 2014, Proc. SPIE, 9147, 91471D
Pesenti, N., Dougados, C., Cabrit, S., et al. 2003, A&A, 410, 155
Pineda, J. E., Offner, S. S. R., Parker, R. J., et al. 2015, Natur, 518, 213
Polomski, E. F., Telesco, C. M., Piña, R., & Schulz, B. 2002, AJ, 124, 2207
Pyo, T.-S., Hayashi, M., Kobayashi, N., et al. 2002, ApJ, 570, 724
Ray, T. P., Poetzel, R., Solf, J., & Mundt, R. 1990, ApJL, 357, L45
Reipurth, B., Clarke, C. J., Boss, A. P., et al. 2014, in Protostars and Planets VI, ed. H. Beuther et al. (Tucson, AZ: Univ. Arizona Press), 267
Rieke, G. H., & Lebofsky, M. J. 1985, ApJ, 288, 618
Rodriguez, L. F., Haschick, A. D., Torrelles, J. M., & Myers, P. C. 1987, A&A, 186, 319
Rosenthal, D., Bertoldi, F., & Drapatz, S. 2000, A&A, 356, 705
Schultz, A. S. B., Rank, D., Temi, P., & Harker, D. 1995, Ap&SS, 233, 71
Shevchenko, V. S., & Yakubov, S. D. 1989, AZh, 66, 718
Skinner, S. L., Brown, A., & Stewart, R. T. 1993, ApJS, 87, 217
Smith, M. D. 1991, MNRAS, 253, 175
Smith, M. D. 1995, A&A, 296, 789
Strom, S. E., Strom, K. M., Yost, J., Carrasco, L., & Grasdalen, G. 1972, ApJ, 173, 353
Takami, M., Chrysostomou, A., Ray, T. P., et al. 2006, ApJ, 641, 357
Tofani, G., Felli, M., Taylor, G. B., & Hunter, T. R. 1995, A&AS, 112, 299
Torrelles, J. M., Curiel, S., Estalella, R., et al. 2014, MNRAS, 442, 148
Trinidad, M. A., Curiel, S., Torrelles, J. M., et al. 2004, ApJ, 613, 416
Turner, J., Kirby-Docken, K., & Dalgarno, A. 1977, ApJS, 35, 281
Weintraub, D. A., Kastner, J. H., & Mahesh, A. 1994, ApJL, 420, L87
Wilking, B. A., Mundy, L. G., & Schwartz, R. D. 1986, ApJL, 303, L61
Yuk, I.-S., Jaffe, D. T., Barnes, S., et al. 2010, Proc. SPIE, 7735, 77351M